

Effect of Si₃N₄ Addition on the Morphological and Structural Properties of the 316L Stainless Steel for Nuclear Applications

Haroune Rachid Ben Zine^{1,2*}, Filiz Cinar Sahin³, Zsolt E. Horváth², Zsolt Czigány²,
Ákos Horváth², Katalin Balázi² and Csaba Balázi²

¹Doctoral School of Materials Science and Technologies, Óbuda University, Bécsi str. 96/B, Budapest, Hungary

²Centre for Energy Research, Hungarian Academy of Sciences, Konkoly-Thege M. str. 29-33, Budapest, Hungary

³Department of Metallurgical and Materials Engineering, Istanbul Technical University, Maslak, Istanbul 34469, Turkey

Received: 25 October 2017; accepted: 05 December 2017

The effect of the submicrometer-sized Si₃N₄ addition on the morphological and structural properties of the ceramic dispersion strengthened (CDS) 316L stainless steels prepared by powder technology has been studied. Two composites were prepared: 316L/0.33 wt. % Si₃N₄ and 316L/1 wt. % Si₃N₄. In order to assure a good dispersion of the ceramic particles in the stainless steel powders and a grain size reduction at the same time, the high efficient attrition milling has been used. Spark plasma sintering (SPS) was used for fast compacting of milled composites. Structural and morphological changes were studied after milling and sintering process. It was found that the amount of Si₃N₄ addition influenced the efficiency of milling process resulting in powder mixtures with different 316L stainless steel grain size and shapes. In the case of 0.33 wt. % Si₃N₄ addition, the flat 316L stainless steel grains with submicrometer size in thickness have been resulted after milling compared to 1 wt. % Si₃N₄ added powder mixtures which consisted of almost globular 316L stainless steel grains with 50–100 μm in diameter. The intensive milling assured an optimal coverage of 316L stainless grains with Si₃N₄ submicrometer-sized particles in both cases as demonstrated by energy dispersive spectroscopy (EDS) and TEM. On the other hand, the 316L phase has been maintained during and after the milling and sintering. The partial phase transformation of α-Si₃N₄ to SiO_x was observed by EDS.

Keywords: Ceramic dispersion strengthened 316L stainless steels, spark plasma sintering, attrition milling, structure, morphology

1. Introduction

316L Austenitic stainless steel has attracted attention due to its good mechanical properties at high temperatures, good corrosion resistance, and good weldability, which can be an effective solution for several industrial applications [1–3]. Cracks-free welding of austenitic metals can be obtained using filler materials with nickel base [3]. The manufacturing route primarily determines the materials properties. Some previous works studied the development of 316L stainless steel powders by using different techniques such as high-power direct laser deposition, selective laser melting (SLM), hot isostatic pressing (HIP), and high-power direct laser deposition (HP DLD) with large size and excellent mechanical properties [4]. Balázi et al. prepared firstly the 316L austenitic stainless steel composites by spark plasma sintering (SPS) [5]. The SLM process provides considerably finer microstructure than the conventionally manufacturing processes [6]. SLM densified specimens have a fine-grained microstructure with elongated grains in build-up direction, but no preferred crystallographic orientation, such as in cast and HIP conditions [7]. During SLM process, the produced samples show different properties in the case of using different combinations of processing parameters even if it is presenting similar energy density [8]. Ziętala et al. studied the properties of the 316L SS fabricated by laser engineering net shaping (LENS) [9]. The study shows that full dense samples without structural defects have been obtained. The samples have a higher content of Mo and Cr in the grain boundaries. A lower Ni content has been observed, which allowed the formation of the delta ferrite on the sub grain boundaries. The sigma-FeCr phase has been observed [9]. This study showed better mechanical and corrosion properties due to the formation of the ferrite phase and the formation of the passive oxide layer, caused by the presence of the chromium in the bulk. The structural characterization shows a heterogeneous

microstructure with elongated austenitic fine grains oriented along the thermocapillary convection direction. This heterogeneous structure of the SS 316L fabricated by LENS had a clear impact on the mechanical properties. The evolution of the structure during the direct laser deposition (DLD) is influenced by the time interval between deposited layers. In the case of long local time intervals, fine microstructures are obtained due to the higher cooling rates. The reduced laser penetration depths result in widespread porosity and less integral metallurgical bonds in locations further upward from the build plate. In the case of the short time intervals, which increases the bulk temperature, samples with coarser structure have been obtained due to lower cooling rates [10]. Zhong et al. studied 316L samples fabricated by electron beam melting for nuclear fusion applications [11]. In their study, the structural characterization show a mixture of irregular shaped sub-grains, solidified melt pools, and columnar grains. Precipitates enriched in Cr and Mo have been observed at the grain boundaries, while no sign of element segregation was shown at the sub-grain boundaries. The porosity in the 316L samples made by powder bed laser fusion is affected by the laser energy density; at high laser energy density, the pores are rounded and randomly distributed, unlike in the case of low laser energy density where the pores are irregular and highly directional [12]. Over 1–5% porosity range angular porosity was found to reduce the Young's modulus by 5% more than rounded porosity [12]. Hajian et al. studied the structural and mechanical properties of friction stir processed 316L stainless steel. They showed that the friction stir process (FSP) exhibited ultrafine grained structures at relatively low rotational speeds [13]. It has been observed that the grain structure evolution of the 316L samples made by FSP was mainly dominated by discontinuous dynamic recrystallization. A significant reduction of twin boundaries fraction in the stir zone was observed in comparison to the base metal. Keller et al. studied the influence of SPS conditions on the sintering and functional properties of an ultra-fine grained 316L stainless steel obtained from ball-milled powder

* Author for correspondence: benzineh@mfa.kfki.hu, bhr.biskra@gmail.com

[14]. The study showed that the use of powder metallurgy technology and the SPS is suitable for the elaboration of AISI SS 316L with ultra fine (UF) grains size. High density values can be obtained by SPS. The elaboration of 316L alloy by ball milling and SPS increases the formation of chromium carbides on the sample surface, also it increases the formation of oxides in the material. These oxides can represent around 10% volume fraction [14]. The sintered samples by SPS has a homogeneous microstructure without preferential grain orientation. The refinement of the grain size increases strongly the samples hardness. In order to improve the properties of the 316L alloy at high temperature for many applications, researchers are using many additives such as Si₃N₄. A study made by Farid et al. [16] showed that the addition of more than 2 wt. % Si₃N₄ to the stainless steel resulted in a decrease in the sintered density and tensile strength values. The Si₃N₄ dissociated to silicon and nitrogen which gives the Ni much higher content than its solubility limit in steel and the nitrogen diffuses out of the matrix leaving pores. In this work, ceramic dispersion strengthened (CDS) steel have been prepared by attritor milling and SPS. The structural and morphological properties have been investigated.

2. Experimental Methods

The composites were prepared from two powders: 316L and Si₃N₄. Commercial austenitic 316L stainless steel from Höganäs consisted of ~70 µm particles with 16.8Cr–12Ni–2.5Mo–1.5Mn–0.6Si composition (Figure 1a). The average size of polygonal α-Si₃N₄ from UBE company is around 200–300 nm (Figure 1b).

The attritor milling (Union Process, type 01-HD/HDDM) has been used for efficient dispersion of submicrometer-sized Si₃N₄ ceramic particles in CDS and for a simultaneously grain size reduction of 316L grains at 600 rpm in ethanol for 5 h. The stainless-steel tank, agitator, and grinding media with 3 mm in diameter have been used for minimalizing of powder contamination.

Spark plasma sintering (Sinter-SPS-7.40MK-VII) was used for sintering of milled powders at 900°C under 50 MPa mechanical pressure for 5 min in vacuum. Sintered solid disks with ~100 mm diameter and ~9 mm thickness have been obtained.

The scanning electron microscopy (SEM, Zeiss-SMT LEO 1540 XB and Jeol JSM-25-SIII) and transmission electron microscopy (TEM, Philips CM-20 with 200 kV acceleration voltage) were used for structural and morphological investigations of base powder, milled, and sintered CDS. The elemental compositions of CDS were measured by energy dispersive spectroscopy (EDS) installed on SEM LEO

microscope. Phase analyses were performed by X-ray diffractometer (XRD, Bruker AXS D8) with CuKα radiation. The hardness of CDS samples was measured by Vickers method 10 N applied load for 10 s.

3. Results and Discussion

3.1. Morphology of Milled Powders and Sintered Composites.

Morphology investigations of milled powders and sintered composites are shown in Figures 2 and 3. The 5-h wet milling induced striking morphological changes of 316L/0.33 wt. % Si₃N₄ grains of powders mixtures. The steel grains transformed from a globular (Figure 1a) to lamellar shape with two typical average sizes (Figure 2a), 100 µm and 40 µm. The Si₃N₄ addition was distributed homogeneously and covered the surface of steel grains (Figure 2b). The morphology of ceramic addition before and after milling is similar, the average size is ~2 times smaller after milling. In the case of 1 wt. % Si₃N₄, the milling was not so effective than in the case of lower ceramic addition. The presence of three grain morphologies was demonstrated: lamellar (~1 µm thin and ~150 µm long), faceted (~25 µm thick and ~50 µm in length), and globular (~50 µm in diameter) (Figure 2c). Due to the milling process, the sub-micrometer Si₃N₄ grains are totally distributed on the 316L grains surface (Figure 2d). The higher amount of ceramic additive prevents the deformation and fracturing of the steel grains during the milling process. Two different effects were observed after milling process. First, the steel grain size reduction efficiency decreased and evolution of flat morphology or shaping of 316L grains is suppressed as the result of Si₃N₄ coverage that behaves like the shielding of each steel particle. On the other hand, the even distribution of ceramic additive is higher. The EDS measurement confirmed the presence of Si₃N₄ in the selected spots (marked by arrows in Figures 2b and d). Figure 2e shows an EDS spectra comparison of 316L stainless steel starting powder and the two prepared mixtures (316L/0.33 wt. % and 1 wt. % Si₃N₄). We noticed two almost similar high peaks of Si and N (due to the presence of Si₃N₄) in both mixtures. The decrease in the peaks intensities of the 316L stainless steel elements (Figure 2e) is due to the good and homogenous coverage of the steel grains by Si₃N₄ particles. The better coverage in the case of 1 wt. % Si₃N₄ resulted in enhanced decrease in the peaks intensities of the 316L grains.

Morphological investigations on fractured surfaces (at room temperature) of sintered 316L/0.33 wt. % Si₃N₄ and 316L/1 wt. % Si₃N₄ after sintering are shown in Figure 3.

In the case of 316L/0.33 wt. % Si₃N₄ (Figures 3a and b), the analysis of the resulting fractured surface after three points

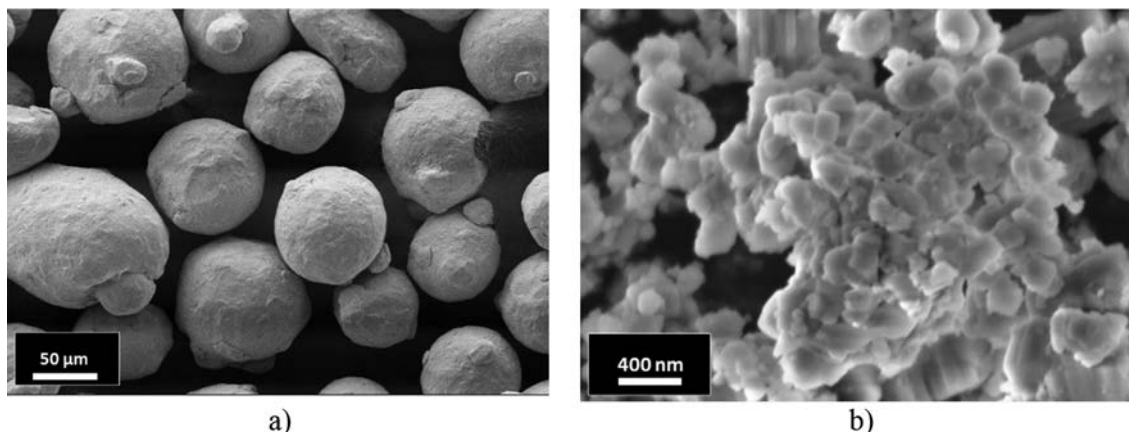


Figure 1. SEM micrographs of starting powders: a) 316L and b) α-Si₃N₄

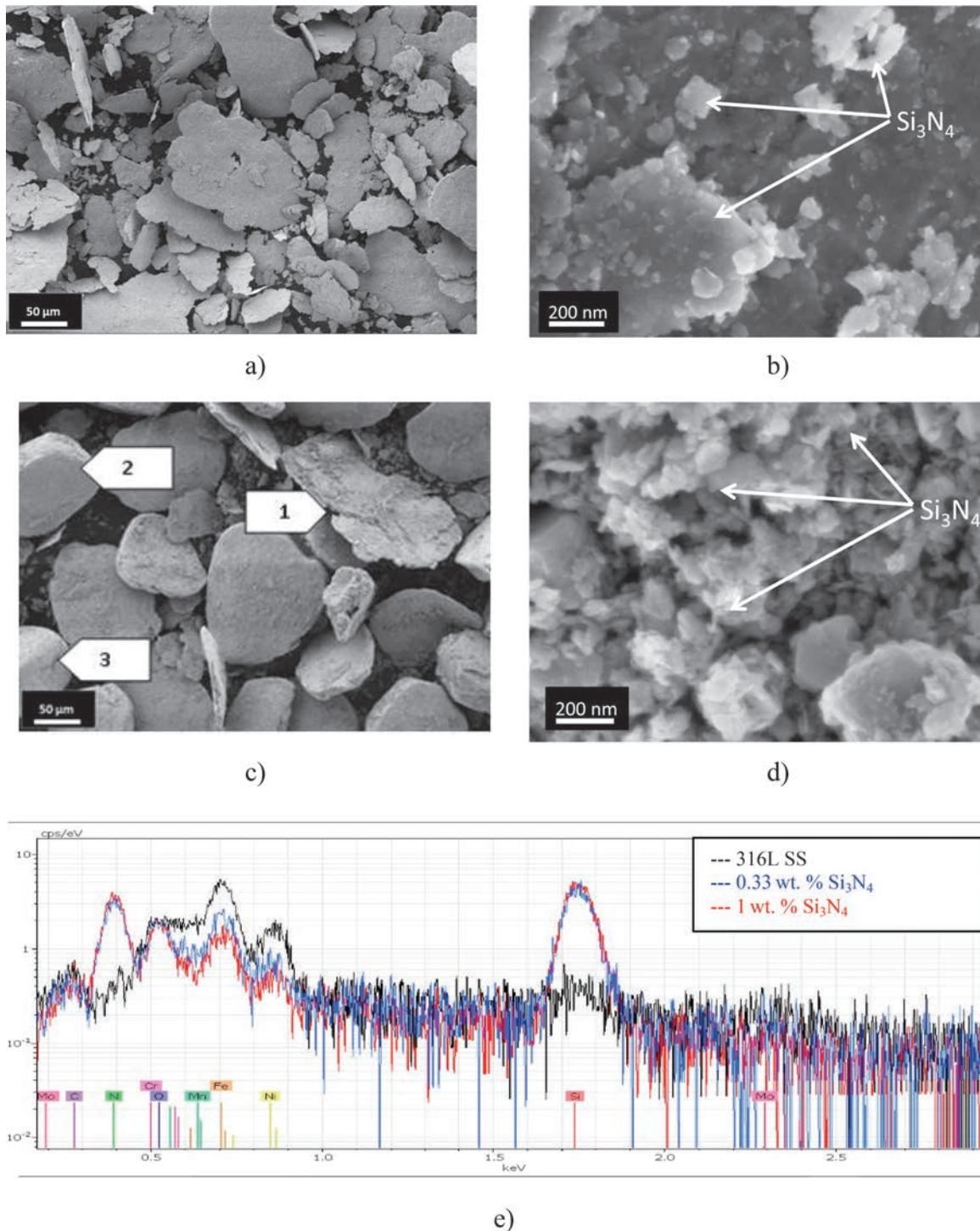


Figure 2. SEM images and EDS spectra of milled powders: a) 316L /0.33 wt. % Si_3N_4 , b) Si_3N_4 distribution on the surface of 316L/0.33 wt. % Si_3N_4 , c) 316L/1 wt. % Si_3N_4 (1, lamellar grain; 2, faceted grain; 3, globular), d) Si_3N_4 distribution on the surface of 316L/1 wt. % Si_3N_4 , and e) comparison of EDS spectra (316L, 316L/0.33 wt. % and 316L/1 wt. % Si_3N_4 powders)

bending test by SEM revealed the dominance of the transgranular fracturing behavior with the presence of intergranular fracturing in some parts. This fracturing behavior is caused by the complex grains boundaries formed by large and thin lamellar grains (Figure 4). In this case, the fracture is propagating both through intergranular or transgranular paths as shown in Figure 4a. Unlike in the case of 1 wt. % Si_3N_4 , the slightly damaged globular grains covered with Si_3N_4 particles clearly affected the fracturing behavior as the SEM images show a dominance of the intergranular fracturing with the presence of very few transgranular fracturing (Figures 3c and d). In this case, the necessary energy for breaking the grains was higher than the necessary energy for contouring them as on Figure 4b.

The average loads given by 3-point bending test were 2627 N for 316L/0.33 wt. % Si_3N_4 whereas 2582 N resulted for 316L/1 wt. % Si_3N_4 composite.

The first mixture (316L/0.33 wt. % Si_3N_4) has been investigated by EDS in order to check presence and the dispersion of the ceramic particles on the surface of the steel grains. The EDS spectra combined with SEM picture with selected spots for EDS are presented in Figure 5. Good dispersion and coverage of the nano-sized ceramic particles (Si_3N_4) on the surface of the stainless-steel grains are shown by SEM and EDS. Spot 1 represents the 316L matrix. Presence of small dark particles (spot numbers 2 and 3) embedded in the steel gains surface is shown by SEM, the EDS spectra show that these dark spots are a mixture of

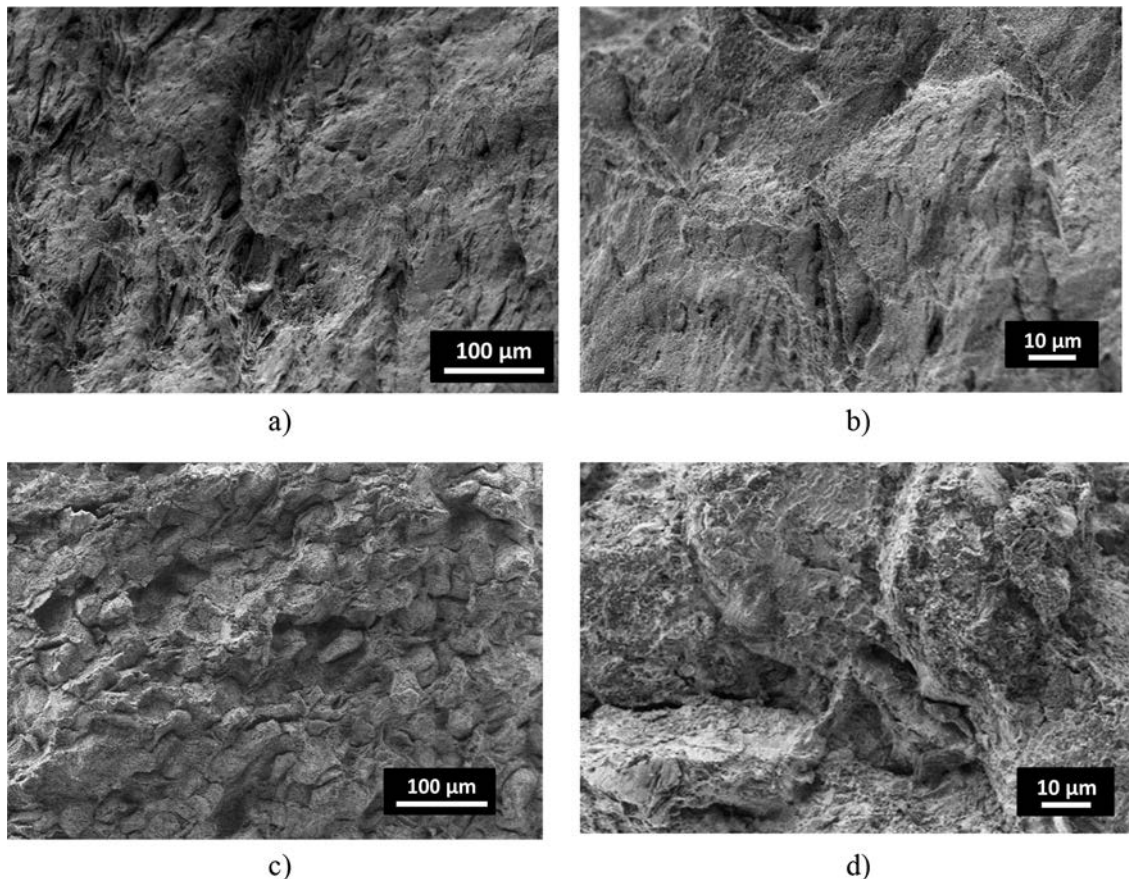


Figure 3. SEM images of sintered composites fractured surfaces: a) and b) CDS with 0.33 wt. % Si₃N₄; c) and d) CDS with 1 wt. % Si₃N₄

Si₃N₄, and oxides are also present (Figure 5). The small bright particles on the grain surface (spot numbers 4 and 5) are steel particles as it is shown in the EDS spectra. In the case of the

second mixture (316L+1wt. % Si₃N₄, Figure 6) we also noticed the good dispersion and coverage of the nano-sized Si₃N₄ on the surface of the stainless-steel grains but with the presence of more

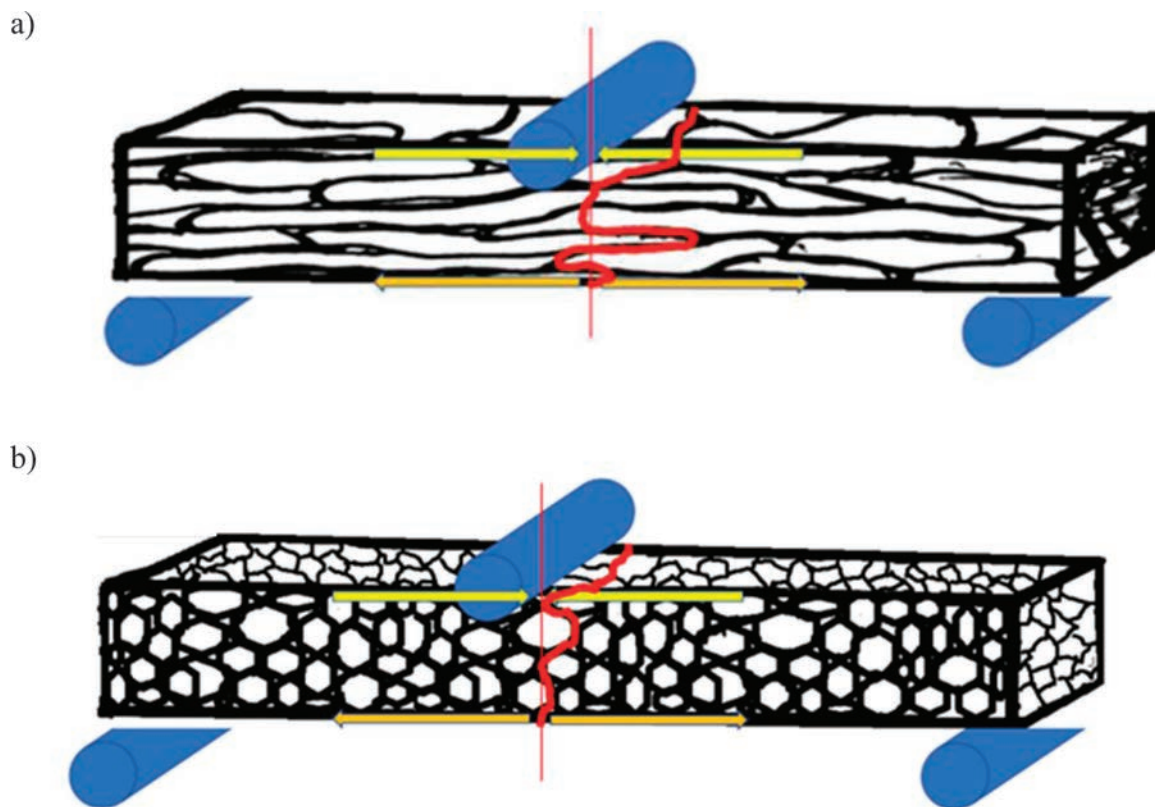


Figure 4. Schematic representation of the dominant fracturing behavior: a) Fracture propagation in the case of the 316L/0.33 wt. % Si₃N₄; b) case of the 316L/1 wt. % Si₃N₄.

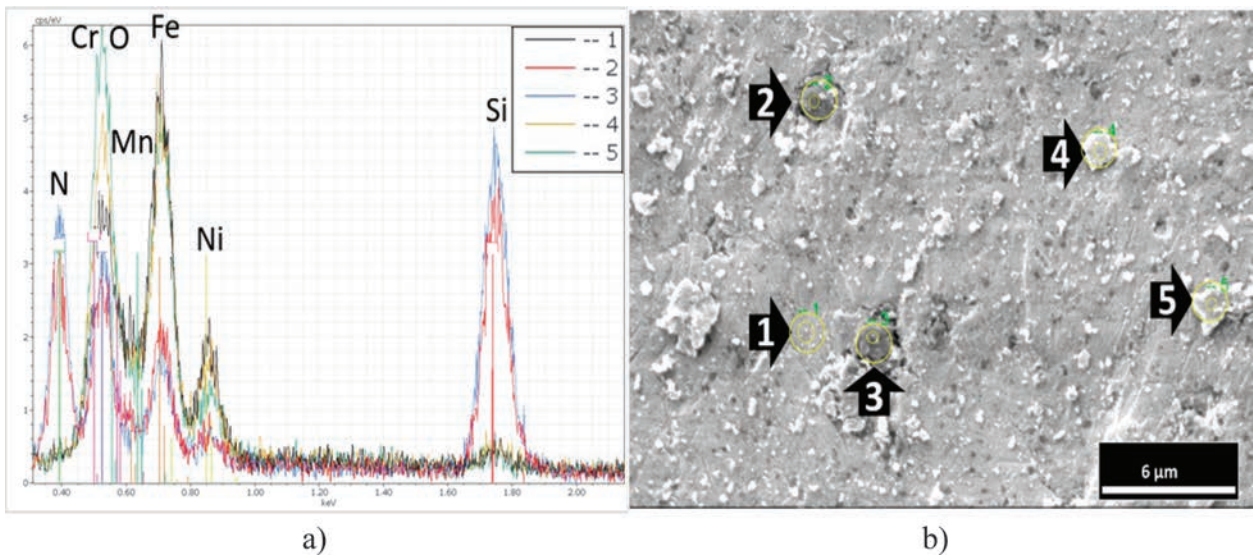


Figure 5. Elemental composition measurements of the 316L/0.33 wt. % Si_3N_4 mixture: a) EDS spectra and b) SEM image

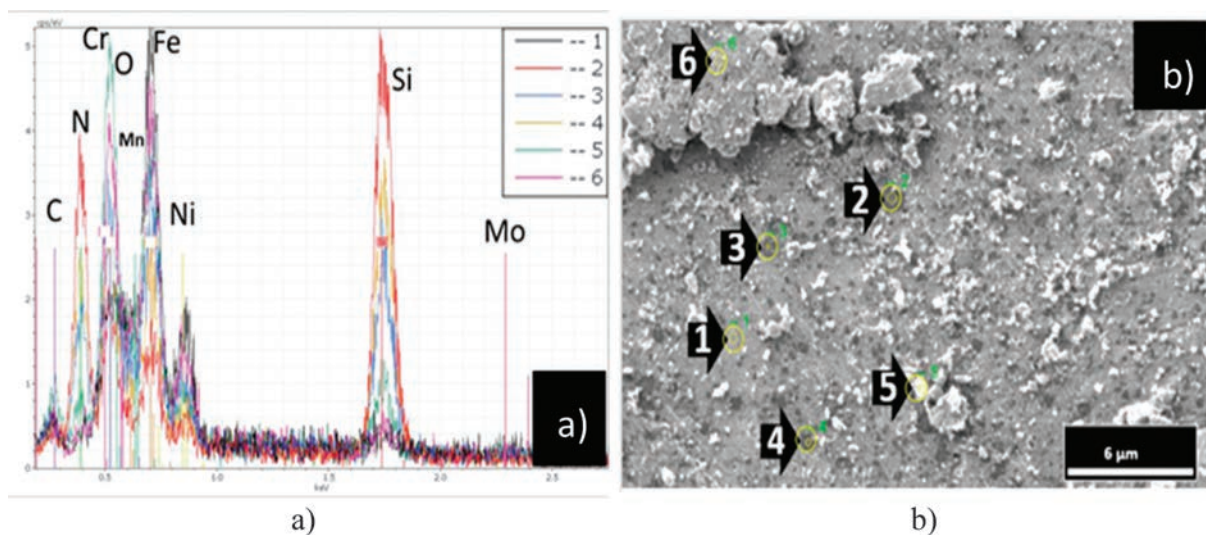


Figure 6. Elemental composition measurements of the 316L/1 wt. % Si_3N_4 mixture: a) EDS spectra and b) SEM image

dark spots (spot number 2, 3, and 4) embedded in the steel grains (spot 1) as it is shown in the Figure 6. The EDS spectra shows that these dark spots are a mixture of Si_3N_4 and possible silicon oxide. The bright spot (number 5) has lower amount of Si_3N_4 and higher amount of oxide phases as shown by EDS.

3.2. Sintered Samples. The EDS spectra (Figure 7a) and SEM image (Figure 7b) are showing the surface of the sintered 316L/0.33 wt. % Si_3N_4 where spot 1 is the 316L matrix and spot 2 is silicon nitride with small amount of oxygen (silicon oxide). The dark phases noted in spot 3 and 5 are silicon oxide with the presence small amount of

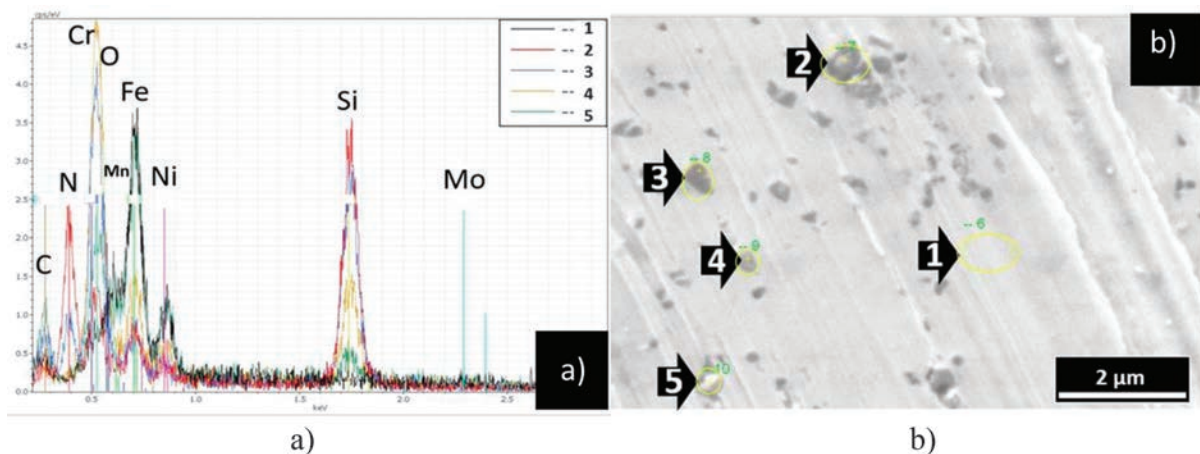


Figure 7. Elemental composition measurements of fracture surface of the 316L/0.33 wt. % Si_3N_4 sintered sample: a) EDS spectra and b) SEM image

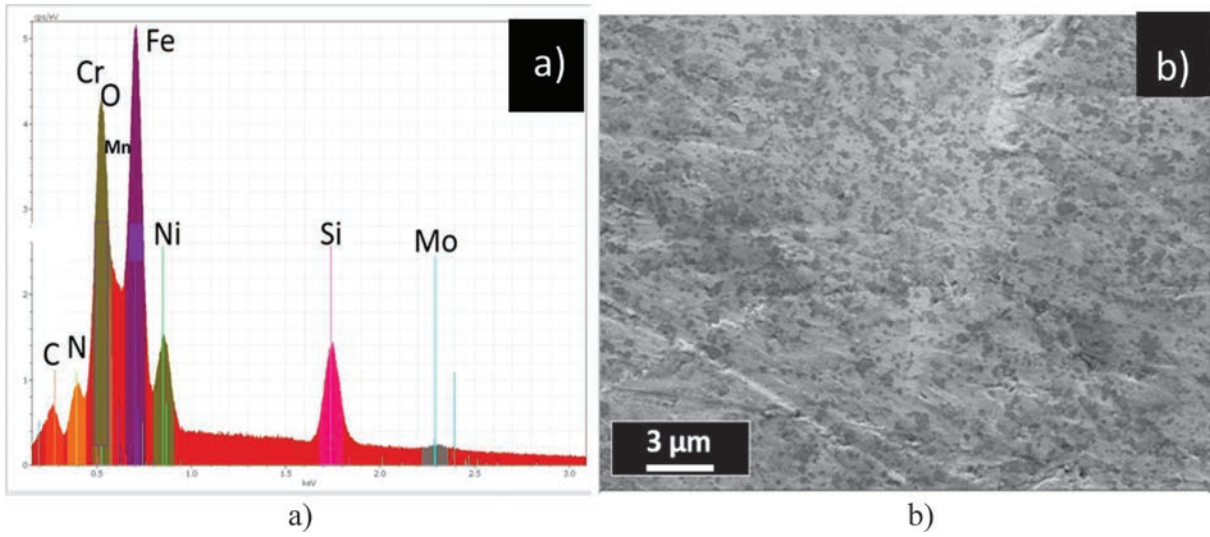


Figure 8. Elemental composition measurements of fracture surface of the 316L/1 wt. % Si₃N₄ sintered sample: a) EDS spectra and b) SEM image

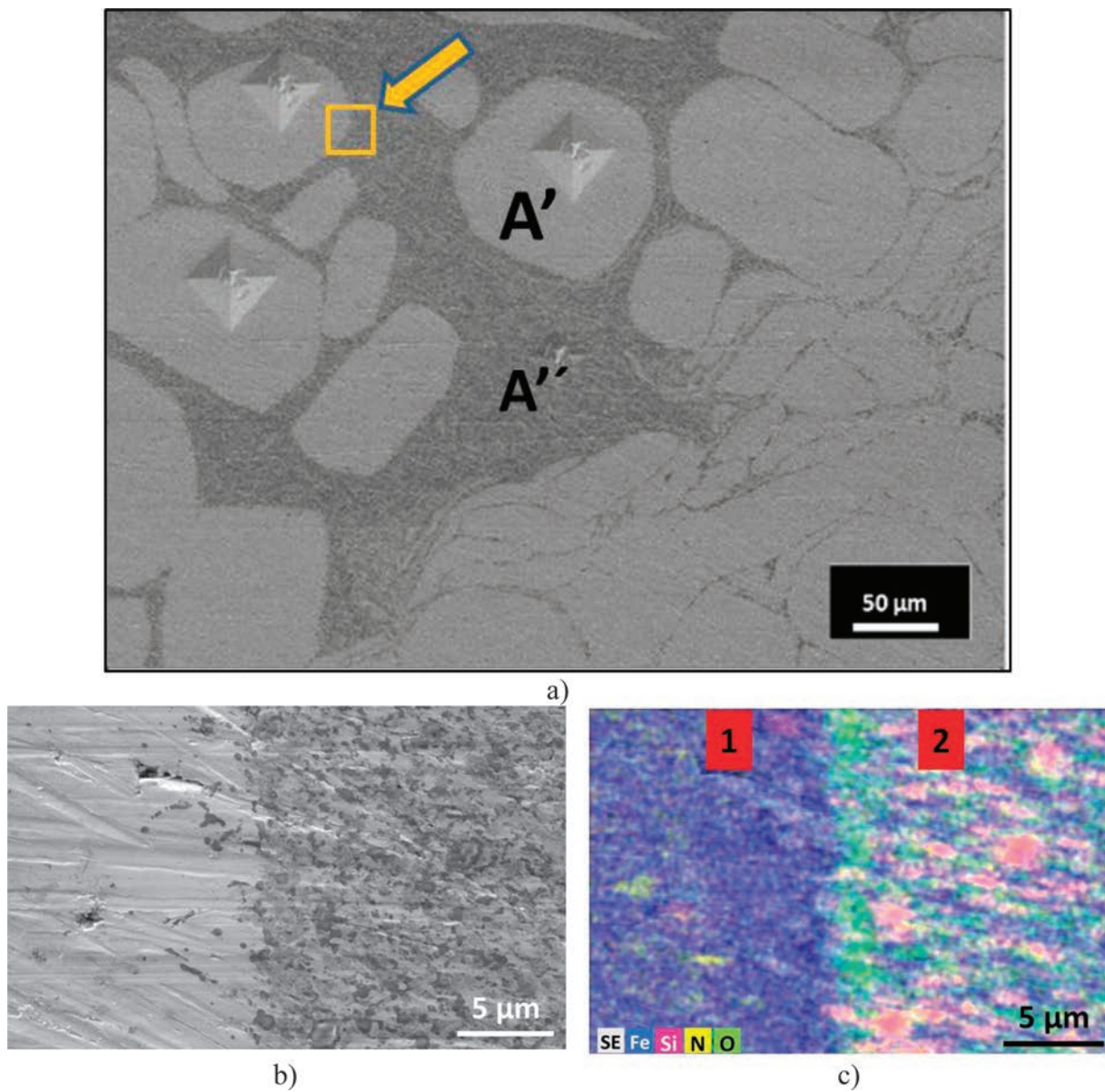


Figure 9. Structural characterization of 316L/1 wt. % Si₃N₄ sintered sample: a) SEM image, b) detail marked by arrow in a), and c) elemental mapping of detailed area in b)

nitrogen and carbon. In spot 4, no nitrogen is detected only silicon and oxygen is showing the presence of an oxide phase. We noticed an increase in the dark spots size due to the agglomeration of the silicon nitride and silicon oxide during the sintering process.

In the case of the 316L/1 wt. % Si_3N_4 , we noticed the increased presence of well distributed dark spots (number 1). The EDS spectra (Figure 8a) and fracture surface observed by SEM (Figure 8b) show the presence of silicon nitride, silicon oxide, and carbon. Figure 9a shows the microstructure of the 316L/1 wt % Si_3N_4 alloy in more detail. We noticed the presence of two different phases (A' and A'') in the SEM images. It is interesting to compare the micro-hardness of the two phases (Figure 9a); an average of $\text{HV} \sim 2.53 \pm 0.17$ GPa has been measured for the A' phase and 7.03 ± 0.41 GPa for the A'' phase. In order to define the two phases and understand the micro-hardness results, we investigated the boundary between the two phases as in the yellow square in the Figure 9a and higher magnification in Figure 9b and using EDS elemental mapping in Figure 9c. The side 1 (A') of Figure 9c shows the austenitic 316L steel with good distribution of silicon, nitrogen, and very small amount of oxygen in it; however, the side 2 (A'') of Figure 9c shows a very high concentration of the silicon, nitrogen,

and oxygen. This means that the dark phase (A'') is a combination of silicon oxide and silicon nitride which explains its higher hardness results.

3.3. X-ray Measurements on Powders and Sintered Samples. The starting powders, the milled powder mixtures, and the sintered samples from the two prepared alloys have been investigated by XRD in order to analyze the present phases. The XRD results are shown in Figure 10. In the case of first alloy (316L/0.33 wt. % Si_3N_4) shown in Figure 10a, the XRD confirmed that the starting powder is austenitic phase of $\gamma\text{-Fe}_3\text{Ni}_2$ phase (JCP2:03-065-5131) with main lines of ($2\theta = 43.532^\circ, 50.705^\circ, 74.535^\circ$). We observed the same $\gamma\text{-Fe}_3\text{Ni}_2$ with the presence of ferrite $\alpha\text{-Fe}$ phase (JCP2: 03-065-4899) after milling of ceramic and steel powders. The presence of this ferrite phase might be due to the contamination from the milling setup (tank, balls, agitator). The very high peak at $2\theta = 69^\circ$ is the Si peak from the sample holder used for XRD measurement. After sintering, the ferrite $\alpha\text{-Fe}$ lines cannot be observed. In the case of the second alloy (316L/1 wt. % Si_3N_4) shown in Figure 10b, the XRD measurement shows that we have the austenite $\gamma\text{-Fe}_3\text{Ni}_2$ phase in the starting powder, the mixture (milled powder), and the sintered sample as well. In this case, there was no $\alpha\text{-Fe}$ lines present on XRD.

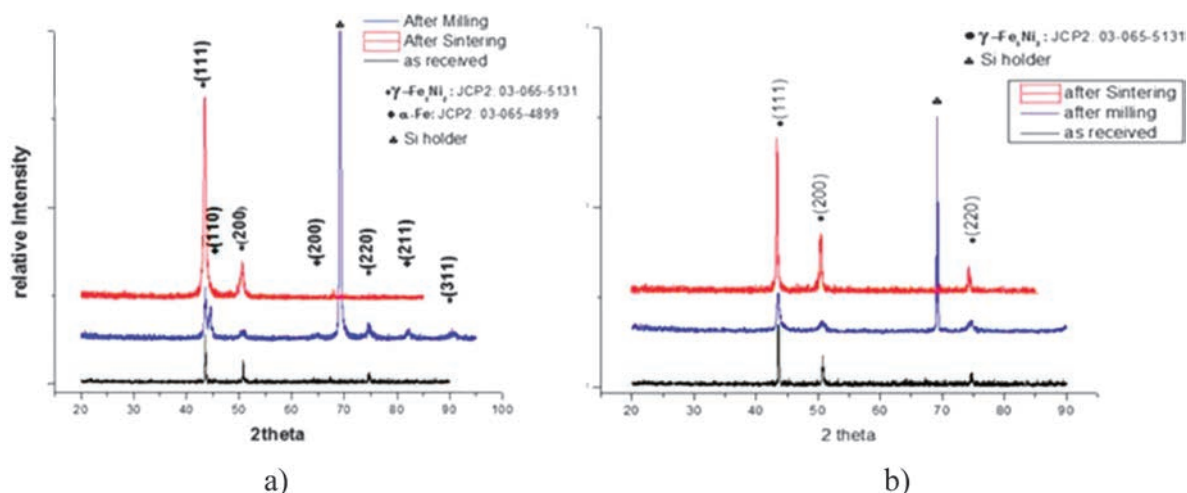


Figure 10. XRD measurement of austenitic powders as received, after milling and after sintering: a) 316L/0.33 wt. % Si_3N_4 ; b) 316L/1 wt. % Si_3N_4

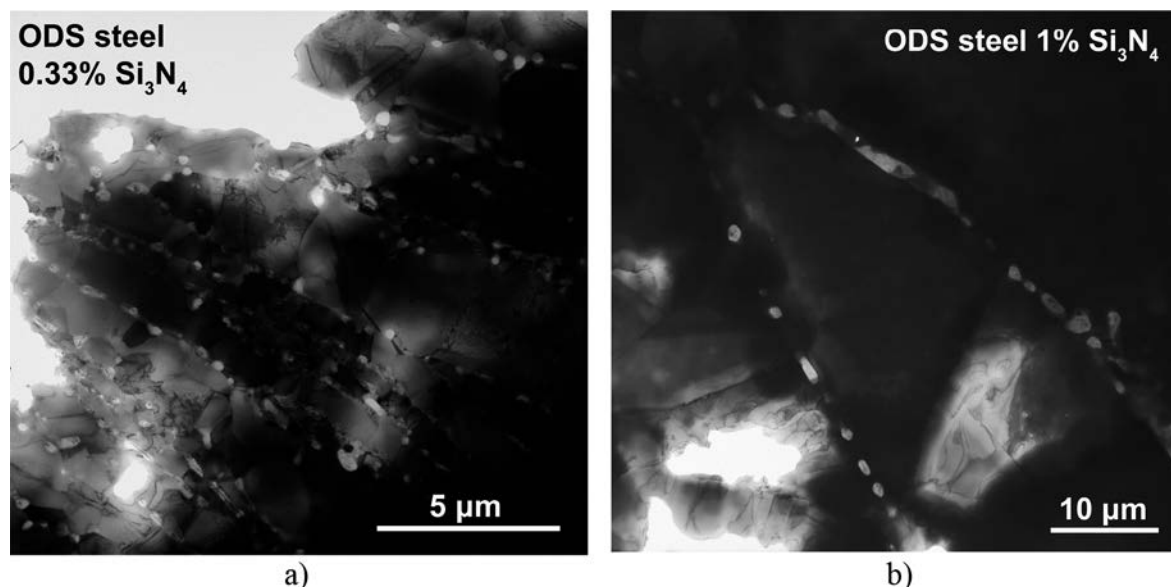


Figure 11. TEM images of sintered samples: a) 316L/0.33 wt. % Si_3N_4 ; b) 316L/1 wt. % Si_3N_4

3.4. Structural Investigations of Sintered Samples.

The structural observations of two sintered samples 316L/0.33 wt. % Si₃N₄ and 316L/1 wt. % Si₃N₄ clearly demonstrate the efficient coverage of steel grains by ceramic particles in both cases (Figure 11). In the case of 316L/0.33 wt. % Si₃N₄ alloy, we obtained a structure with finer grains than for 316L/1 wt. % Si₃N₄ alloy showing a more coarse grain structure. This observation is in agreement with structural observations presented in Figures 2 and 3, Figures 5 and 6, and Figures 8 and 9.

4. Conclusions

The effect of the submicrometer-sized Si₃N₄ addition on the morphological and structural properties of the ceramic dispersion strengthened (CDS) 316L stainless steels prepared by powder technology has been studied. Two composites were prepared: 316L/0.33 wt. % Si₃N₄ and 316L/1 wt. % Si₃N₄. In order to assure a good dispersion of the ceramic particles in the stainless steel powders and a grain size reduction at the same time, the high efficient attrition milling has been used. It has been found that 5 h of milling in ethanol at 600 rpm using 3 mm grinding stainless steel balls was sufficient to obtain grains with flake-like shape in case of 316L/0.33 wt. % Si₃N₄. SPS was used for fast sintering of milled composites. The samples have been sintered under 50 MPa at 900 °C for 5 min in vacuum. Structural and morphological changes were studied after milling and sintering process. It was found that the amount of Si₃N₄ addition influenced the efficiency of milling process resulting in powder mixtures with different 316L stainless steel grain size and shapes. In the case of 0.33 wt. % Si₃N₄ addition, the flat 316L stainless steel grains with submicrometer size in thickness have been resulted after milling compared to 1 wt. % Si₃N₄ added powder mixtures which consisted of almost globular 316L stainless steel grains with 50–100 μm in diameter. The intensive milling assured an optimal coverage of 316L stainless steel grains with Si₃N₄ submicrometer-sized particles in both cases as demonstrated by EDS and TEM. On the other hand, the 316L phase has been maintained during and after the milling and sintering. The partial phase transformation of α-Si₃N₄ to SiO_x was observed during sintering by EDS.

Acknowledgments. Mr. Haroune Rachid Ben Zine thanks Hungaricum Stipendium and MTA EK project “Nanostructural ODS steel development” for support.

Open Access. This is an open-access article distributed under the terms of the Creative Commons Attribution-NonCommercial 4.0 International License (<https://creativecommons.org/licenses/by-nc/4.0/>), which permits unrestricted use, distribution, and reproduction in any medium for non-commercial purposes, provided the original author and source are credited, a link to the CC License is provided, and changes - if any - are indicated.

References

1. Karthik Desu, R.; Krishnamurthy, H. N.; Balu, A.; Kumar Gupta, A.; Kumar Singh, S. *Mater. Res. Technol.* **2016**, *5*, 13–20.
2. Biehler, J.; Hoche, H.; Oechsner, M. *Surf. Coat. Technol.* **2017**, *313*, 40–46.
3. Li, H. L.; Liu, D.; Yan, Y. T.; Guo, N.; Feng, J. C. *J. Mater. Process. Technol.* **2016**, *238*, 423–430.
4. Guo, P.; Zou, B.; Huang, C.; Gao, H. *J. Mater. Process. Technol.* **2017**, *240*, 12–22.
5. Balázs, C.; Gillemot, F.; Horváth, M.; Wéber, F.; Balázs, K.; Sahin, F. C.; Onüralp, Y.; Horváth, Á. *J. Mater. Sci.* **2011**, *46*, 4598–4605.
6. Suryawanshia, J.; Prashanth, K. G.; Ramamurtya, U. *Mat. Sci. Eng. A* **2017**, *696*, 113–121.
7. Röttger, A.; Geenen, K.; Windmann, M.; Binner, F.; Theisen, W. *Mat. Sci. Eng. A* **2016**, *678*, 365–376.
8. Miranda, G.; Faria, S.; Bartolomeu, F.; Pinto, E.; Madeira, S.; Mateus, A.; Carreira, P.; Alves, N.; Silva, F. S.; Carvalho, O. *Mat. Sci. Eng.* **2016**, *A657*, 43–56.
9. Ziętala, M. *Mat. Sci. Eng. A* **2016**, *677*, 1–10.
10. Yadollahi, A.; Shamsaei, N.; Thompson, S. M.; Seely, D. W. *Mat. Sci. Eng. A* **2015**, *644*, 171–183.
11. Zhong, Y.; Rannar, L.-E.; Liu, L.; Koptuyug, A.; Wikman, S.; Olsen, J.; Cui, D.; Shen, Z. *J. Nucl. Mater.* **2017**, *486*, 234–245.
12. Lavery, N. P.; Cherry, J.; Mehmood, S.; Davies, H.; Girling, B.; Sackett, E.; Brown, S. G. R.; Siens, J. *Mat. Sci. Eng. A* **2017**, *693*, 186–213.
13. Hajian, M.; Abdollah-zadeh, A.; Rezaei-Nejad, S. S.; Assadi, H.; Hadavi, S. M. M.; Chung, K.; Shokouhimehr, M. *Mater. Des.* **2015**, *67*, 82–94.
14. Keller, C.; Tabalaiev, K.; Mamier, G.; Noudem, J.; Sauvage, X.; Hug, E. *Mat. Sci. Eng.* **2016**, *A665*, 125–134.
15. Akhtar, F.; Peizhong, F.; Xueli, D.; Askari, S. J.; Jianjun, T.; Shiju, G. *Mat. Sci. Eng. A* **2008**, *472*, 324–331.
16. Ceniga, L. *J. Thermal Stresses* **2004**, *27*, 471–489.
17. Siska, F.; Stratil, L.; Hadraba, H.; Fintova, S.; Kubena, I.; Zalezak, T.; Bartkova, D. *Mat. Sci. Eng. A* **2017**, *689*, 34–39.